ASTEROID PROXIMITY GNC ASSESSMENT THROUGH HIGH-FIDELITY ASTEROID DEFLECTION EVALUATION SOFTWARE (HADES)

Massimo Vetrisano and Juan L. Cano

Deimos Space S.L.U., Ronda de Poniente, 19, 28760 Tres Cantos, Madrid, Spain, *+34 918063450*, *{massimo.vetrisano, juan-luis.cano}@deimos-space.com*

ABSTRACT

The High-fidelity Asteroid Deflection Evaluation Software (HADES) deals with the high-fidelity modelling of spacecraft operations at irregular shape asteroids.

The software can handle any operational orbit, with particular care paid to inertial and body fixed hovering. Different control techniques based on both continuous and discrete methods have been considered and implemented. The manoeuvre execution itself can be affected by errors in magnitude and direction.

The spacecraft orbit determination is performed through a performance model or by on-board measurements, a navigation camera and a LIDAR, which are processed by an Unscented H-infinity Filter (UHF). HADES can employ different levels of accuracy between the assumed environment knowledge and the real world.

HADES comes with a Monte Carlo (MC) module which allows drawing more noticeable statistical parameters. Also HADES contains preliminary asteroid deflection capabilities where low push methods, i.e. laser ablation, ion-beam shepherd and gravity tractor have been included.

Index Terms— Asteroid Proximity, GNC, Inertial Hovering, Body Fixed Hovering, Non-uniform Gravity field, Optimal Control, Unscented H-infinity Filtering, Asteroid Deflection, Laser Ablation, Ion Beam Shepherd, Gravity Tractor.

1. INTRODUCTION

In the last 20 years, there has been considerable progress in the exploration of the minor celestial objects by spacecraft. Recently the most remarkable mission has been Rosetta, which arrived at Comet 67P/Churyumov–Gerasimenko on 6 August 2014. The lander Philae achieved the first-ever soft landing on the surface of the comet on 12 November 2014. As shown by the difficulties on the identification of the final landing spot of the probe, the environment near minor bodies is pretty complex because of the lack of precise data where simplification regarding the shape and composition of the asteroid can drive to a completely incorrect picture of the dynamics.

The navigation in close proximity of asteroids can be complicated due to the fact that the environment is uncertain, especially if the asteroid presents an irregular shape and rotation state. The motion of the spacecraft around the asteroid is, thus, highly nonlinear.

Generally, the gravitational harmonics of the celestial minor bodies are estimated from on-board data collected during a close fly-by [1], during approach phases [2] or by ground-based radar imaging data [3]. Thus, it is necessary to evaluate possible different navigation strategies to increase the mission reliability and the possibility to cope with both unknown environment and system performance uncertainties.

For this purpose the High-fidelity Asteroid Deflection Evaluation Software, HADES, has been under development at Deimos Space. HADES is a high-fidelity simulation tool working in Matlab® to assess GNC close proximity operations. Detailed models about the close proximity environment about Near Earth asteroids (NEA) and the involved operations are required during preliminary assessment of mission requirements especially under the presence of uncertainties. The implemented spacecraft dynamics considers the most relevant perturbations, i.e. third body effect from the Sun, solar radiation pressure (SRP) and irregular gravity field of the rotating asteroid. The software uses both spherical harmonics and actual asteroid's shape. In the first case the coefficients can be given from actual data or they are calculated on a user-defined ellipsoid; in the second case the gravity field is reconstructed from the asteroid tetrahedral mesh. The software can handle any operational orbit, with particular care paid to inertial and body fixed hovering.

One important aspect when designing proximity operations is to evaluate how the different control techniques and on-board instruments affect the performance of the system. Different control techniques based on both continuous and discrete methods have been considered and implemented. The manoeuvre execution itself can be affected by errors in magnitude and direction.

This kind of missions typically requires the spacecraft to fly in a tight formation relatively close to the asteroid, so on-board estimation capabilities are desirable and indeed required when the delay time between ground and the spacecraft is too high to ensure the safety of operations.

Methods based on optical navigation camera and laser light radar (LIDAR) or laser range finder (LRF) integrated measurements have been proved to be a feasible option for a single spacecraft to approach or land on an asteroid [4][5]. HADES has a detailed model of camera and LIDAR, where the actual illumination and visibility conditions are modelled using real asteroid shape data.

Currently, HADES can also perform preliminary asteroid deflection mission analysis. Different methods have been proposed and studied to deflect potentially hazardous asteroid [6][7]. In theory, with enough warning time the slow push techniques will enable the deflection while carrying also scientific objectives. In fact, in contrary to asteroid impactor or nuclear blast techniques, these will not require the destruction of the probe during the mission while eliminating the need for a second precursor probe (see current AIM mission [8]). HADES contains a suite which allows calculating preliminary performance of the laser ablation, ion-beam shepherd and gravity tractor techniques. The integration of the GNC system is under development and will be matter of the final HADES version.

This paper is organised as follows. Section 2 explains the different dynamics model and main modelisation. In Section 3, the control techniques used to maintain the spacecraft on its reference trajectory are briefly explained. Section 4 shows the estimation process through the Unscented H-Infinity filter and the assumed measurements model. Section 5 describes the deflection process through the laser ablation, ion-beam shepherd and gravity tractor slow push methods. Finally Section 6 shows the results. In particular all the analyses for the GNC case are applied to the case of the asteroid Didymos, which is the object of the AIM mission [8], while a short comparison on the implemented deflective techniques focuses on a 100 m actual shape asteroid. A short debris analysis is also carried out.

2. DYNAMICS MODELS

HADES relies on a number of different dynamics models.

2.1. Hill's reference frame dynamics

In this section, we introduce the motion dynamics of spacecraft and asteroid in the quasi-inertial Hill's reference Frame (see Figure 1(1)). It is assumed that the asteroid body frame (later described) is coincident with this frame at the beginning of the simulations.

The spacecraft is subjected to the force due to solar gravity, solar radiation pressure and the asteroid's irregular gravity.

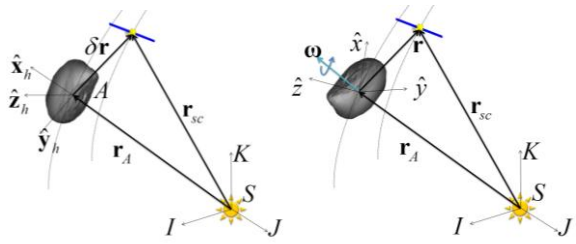

Figure 1. 1) Hill's reference frame, 2) body fixed reference frame.

The nonlinear relative equations of motion are given by [9]:

$$\ddot{\mathbf{r}} + 2\dot{\boldsymbol{\theta}}\mathrm{x}\dot{\mathbf{r}} + \dot{\boldsymbol{\theta}}\mathbf{x}\left(\dot{\boldsymbol{\theta}}\mathbf{x}\mathbf{r}\right) = -\frac{\mu_a}{r^3}\mathbf{r} + \mu_{\mathrm{Sun}}\left(\frac{\mathbf{r_a}}{\mathbf{r_a^3}} - \frac{\mathbf{r_{sc}}}{\mathbf{r_{sc}^3}}\right) + \frac{\partial U}{\partial(\boldsymbol{\delta r})} + \boldsymbol{SRP}(\mathbf{r_{sc}}) + \mathbf{u} \quad (1)$$

with μ_{Sun} is the Sun gravity constant, μ_a is the gravity constant of the asteroid, r_a and r_{sc} are the positions of the asteroid and spacecraft with respect to the sun. $\boldsymbol{r}$ is the relative distance between spacecraft and asteroid. $\dot{\boldsymbol{\theta}}$ represents the instantaneous angular velocity with which the asteroid (i.e. the reference frame) rotates around the Sun. $SRP(\boldsymbol{r_{sc}})$ is the solar radiation pressure; $\mathbf{u} = [\boldsymbol{u_x}, \boldsymbol{u_y}, \boldsymbol{u_z}]$ is a control input for continuous control. In the case of impulsive control this term is null and impulsive variation of velocity is applied at the time of the manoeuvre. U is the higher order potential of the asteroid.

2.2. Asteroid's inertial frame dynamics

The equations of motion are described in the asteroid ecliptic reference frame. It is assumed that the asteroid body frame is coincident with this frame at the beginning of the simulations.

In this case the nonlinear relative equations of motion are given by [9]:

$$\ddot{\boldsymbol{r}} = -\frac{\mu_a}{\delta r^3}\boldsymbol{r} + \mu_{Sun}\left(\frac{\boldsymbol{r_a}}{r_a^3} - \frac{\boldsymbol{r_{sc}}}{r_{sc}^3}\right) + \frac{\partial U}{\partial(\delta \boldsymbol{r})} + SRP(\boldsymbol{r_{sc}}) + \boldsymbol{u} \quad (2)$$

where all the terms have the same meaning of the previous section but in the asteroid ecliptic reference frame.

2.3. Body fixed dynamics

In this section, we introduce the motion dynamics of spacecraft and asteroid in the non-inertial body frame (see Figure 1(1)). The nonlinear relative equations of motion are given by [9]:

$$\ddot{\mathbf{r}} + 2\boldsymbol{\omega}\mathbf{x}\dot{\mathbf{r}} + \boldsymbol{\omega}\mathbf{x}(\boldsymbol{\omega}\mathbf{x}\mathbf{r}) = -\frac{\mu_a}{r^3}\mathbf{r} + \mu_{Sun}\left(\frac{\mathbf{r_a}}{\mathbf{r_a^3}} - \frac{\mathbf{r_{sc}}}{\mathbf{r_{sc}^3}}\right) + \frac{\partial U}{\partial(\boldsymbol{\delta}\mathbf{r})} + \boldsymbol{SRP}(\mathbf{r_{sc}}) + \mathbf{u} \quad (3)$$

and $\boldsymbol{\omega}$ is the angular velocity. For simplicity it was assumed that the asteroid rotates around its minor axis of inertia, which means the asteroid rotates in its equatorial plane.

2.4. Gravity field through spherical harmonics

The asphericity of these bodies gives raise to perturbations that affect all orbital elements, especially at low altitude. The model that has been considered to describe these effects is based on the standard Legendre polynomials of the gravity field potential as defined by Cunningham [10]. The model works nicely when outside the object circumscribing sphere while inside it is completely unreliable. The use of Legendre polynomials allows an efficient computation of the potentials and resulting perturbation as a function of the Cartesian coordinates in the body fixed reference frame.

The second method of gravity model works for an arbitrary shape and was implemented from the equations used in [11]. This model assumes a uniform density of the asteroid and allows expressing the local acceleration in an arbitrary location of space with respect to the asteroid's centre of mass. It is especially suited for proximity operations, where the harmonic techniques fail to provide an accurate representation of the gravity field.

As an example Figure 2 shows the error between the harmonics gravity field and the shape based model on the circumscribing sphere around a tri-axial ellipsoid of semi-axes [3, 2, 0.5] km.

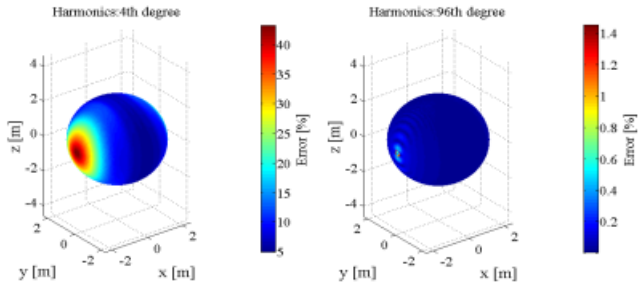

Figure 2. Error between harmonics and shape model gravity field on the asteroid circumscribing sphere.

In the case of harmonics an analytical formula for calculating the even terms of the matrix $\boldsymbol{C}$ was obtained from [12] as a function of c_1, c_2 and c_3, the semi-axes of a tri-axial ellipsoid.

A 4th order gravity field produces a relative error up to 40% along c_1, while a 96th is pretty much coincident with the shape model.

3. CONTROLLERS

The implemented controllers consist of continuous and discrete control logics. The orbital plane velocity is such that the Coriolis contribution can be neglected. In this way the controllers needs to be specialised simply for inertial and body fixed cases. Moreover, during the development of the software it was found that some control logics were not applicable to the different analysed dynamics and some did not produce any gain from an efficient point of view (imprecise and expansive).

Following control methods have been implemented in this first release of the software release:

1. A continuous Lyapunov controller
2. Discrete controllers based on the concept of control box
3. Discrete control based on reflection method
4. Discrete control based on dead band control
5. Discrete LQR with integrative contribution
6. Discrete control designed using stability criteria

The last controller was successfully implemented only for the inertial dynamics problem.

3.1. Continuous controller– Lyapunov controller

Solar radiation pressure and central gravity field are major perturbative forces, while the inhomogeneous gravity of the asteroid and any other non-spherical terms in the gravity field expansion result in only small perturbations, then a simple control law based on the Lyapunov control function can be built up [13]:

It is assumed that the motion along the reference formation orbit is much slower than the control action.

$$\boldsymbol{u} = -\left(-\frac{\mu_a}{\delta r_{\text{est}}^3}\delta\boldsymbol{r}_{\text{est}} + SRP(\delta\boldsymbol{r}_{\text{SC-est}})\right) - \mathrm{c}_p\left(\delta\boldsymbol{r}_{\text{est}} - \delta\boldsymbol{r}_{\text{ref}}\right) - c_{\mathrm{v}}\left(\delta\boldsymbol{v}_{\text{est}} - \delta\boldsymbol{v}_{\text{ref}}\right) \quad (4)$$

All the quantities with subscript *est* refer to estimated variables. In case of the body frame, the Coriolis effects were included. The first term of Eq. (4) deals with the perturbations, while the second and third terms apply am action proportional to the state error. c_p and c_d will depend on the dynamics itself. In order to avoid tuning this parameters manually, one suitable choice is to use a Linear Quadratic Regulator (LQR). We use the Matlab®'s lqr function for this.

Although this method is continuous for easiness of implementation, it was reduced to a sort of patched continuous method. A continuous thrust based on constant errors was applied between two consecutive intervals of time when the measurements are received.

3.2. Discrete controllers

3.2.1. Control box

The controller implemented is discrete on per component basis through a control box of size l . A delta manoeuvre is performed when the error along a component is higher than the side of the box.

The manoeuvre is calculated assuming a constant acceleration from the central gravity field, such that a linearized motion can be described.

3.2.2. Reflection & inversion methods

The method consists in reflecting the relative velocity applying a delta-v in the inertial direction (see page 248 of [9]), when the spacecraft get closer to the asteroid, along that inertial direction. It is not meant to be a tight control, and maintain the spacecraft within delimited boundary. It is only to avoid the spacecraft from getting closer to the asteroid and eventually colliding with it. The lower limit is calculated as for the control box. The following option was considered:

1. inverting the direction of the velocity when the spacecraft gets closer;
2. applying a delta-v manoeuvre along the radial direction such as to obtain the velocity reflected with respect to the tangential direction.

With no errors the resultant velocity will maintain the same magnitude of the initial velocity. In both cases a dissipative coefficients of 0.95 on the magnitude of the correction manoeuvre was used. Dissipating energy is preferable to increasing it, which has the effect of destabilising the controlled trajectory.

3.2.3. Dead band

Depending on allowable region in which the spacecraft is confined, dead band control could be actually seen as part of the control box family. It is preferred here to treat it separately, because instead of controlling all the directions, only two directions were bounded, those are the ones perpendicular to the Sun-asteroid direction. This choice was driven by the work of [14]. In practice, it is required that the dead-band correction manoeuvre be normal to the dead-band boundary.

Care must be given to the fact that the method in [14] was devised for time invariant systems, and the boundness of the spacecraft motion will not be assured when the higher order harmonics are taken into account. For this reason we introduced a dissipating part of the kinetic energy during the correction manoeuvre. A corrective factor of 0.95 was then applied to take into account the time-variability and the errors from the both the control and the orbit determination.

An additional contribution was indeed foreseen to address the motion of the reference point in the case of the boxy fixed dynamics. This was calculated 'offline' independently from the measurement process. The aim was to find an optimal manoeuvre (i.e. minimising the delta-v) which would bound the motion of the reference point between two subsequent instants of time. The contribution is calculated assuming a constant acceleration:

$$\min \Delta v_{\mathrm{ref}} \text{ s.t. } \mathbf{r}_{\mathrm{ref}}(t_0 + \Delta t) - r_{\mathrm{ref}}(t_0 + \Delta t) = 0 \qquad (5)$$

Where the motion was calculated neglecting the effects from the SRP and Sun gravity field. In this way the manoeuvre is a constant, being independent from the relative position of the Sun with respect to the spacecraft.

3.2.4. LQR with integrative contribution

Similarly to the problem of continuous thrust, we want to calculate the optimal gain matrix $\mathbf{K}$ such that the state-feedback law $\mathbf{u_k} = -\mathbf{K}\delta\mathbf{x_k}$ (where k is the discrete step).

Although the controller will work using only proportional correction manoeuvre, we decided to add the integrative contribution due to the action of the gravity field during the interval between corrections. The integrative contribution improves the accuracy because otherwise the spacecraft will tend to move towards an artificial equilibrium point where

$$\frac{c_p}{c_d} = -\frac{\delta v_{est} - \delta v_{ref}}{\delta r_{est} - \delta r_{ref}}$$

We assume that the overall effect from the other forces is negligible and the LQR is able to cope with those perturbations. The integrative contribution is calculated assuming a constant acceleration:

$$\boldsymbol{u_k} = -\boldsymbol{K}\delta\boldsymbol{x_k} - \bar{a}_{\mathrm{p}}\Delta t\hat{\boldsymbol{r}}_{\boldsymbol{0}} \qquad (6)$$

where $\bar{a}_{\mathrm{p}}$ is the mean value of acceleration as measured at centre, superior and inferior edge of the control box. The integrative contribution was added only when contribution of the perturbations does not work to reduce the position error. This is done simply to include the fact that the gravity acts favourably by attracting the spacecraft towards the reference position when the spacecraft is above the nominal altitude.

3.2.5. Stable discrete controller

The design of the following stable controller is based on the work of [15]. The main findings of this work are given in order to understand the subsequent steps.

Two functions correspond to the dynamics and to an observer of the system:

$$\begin{array}{ll} \dot{\mathbf{x}} = f(t,\boldsymbol{x}) & t \neq t_k \\ \mathbf{z} = h(\mathbf{x}) & t \neq t_k \\ \Delta\mathbf{x} = \mathbf{u_k}(\mathbf{x}) & t = t_k \\ \mathbf{x}(\mathrm{t}_0) = \mathbf{x}_0 & t = t_0 \end{array} \quad (7)$$

The method requires that the function *f* and *h* are null for $\boldsymbol{x} = \mathbf{0}$, so a linearized version of the equation around the nominal initial state $\boldsymbol{r_0}$ was used for the inertial/hill dynamics. Neglecting the contribution of the Coriolis forces, one can use the discrete equations of motion of Eq.(2):

$$\dot{\delta\mathbf{x}} = \begin{bmatrix} \mathbf{0_{3x3}} & \boldsymbol{I_{3x3}} \\ -\frac{\mu_a}{\delta r_0^3}[\boldsymbol{I} - 3\hat{\mathbf{r}}_0\hat{\mathbf{r}}_0] & \mathbf{0_{3x3}} \end{bmatrix}\delta\boldsymbol{x} = \begin{bmatrix} \mathbf{0_{3x3}} & \boldsymbol{I_{3x3}} \\ \boldsymbol{\beta} & \mathbf{0_{3x3}} \end{bmatrix}\delta\boldsymbol{x} \quad (8)$$
$$\mathbf{z} = \delta\boldsymbol{x}$$

In order to obtain a stable controller following this method we need first to define a function of the state variables, positive definite, in the form of

$$V(t,\boldsymbol{x}) \leq a(\|\boldsymbol{x}\|) \quad (9)$$

Where a is a suitable positive coefficient, $\boldsymbol{x}$ is the state vector. According to the paper the main conditions for the stability require

1. There has to exist a constant l_k such that

$$D^+V(t,\boldsymbol{x}) \leq \frac{l_k}{\Delta t_k} c_k\big(V(t,\boldsymbol{x})\big) \quad (10)$$

where D^+ is the right-hand generalized derivative, Δt_k is the time interval between two subsequent control inputs. $c_k(\ldots)$ is a suitable scalar function.

2. There has to exist a constant v_k such that

$$\boldsymbol{V}(t_k^+, x + u_k) \leq V\big(t_k\ , x\big) + v_k d_k(V(t,x)) \quad (11)$$
$$l_k + v_k\ \leq 0 \quad (12)$$

for suitable neighbourhood of $\boldsymbol{x}$ $(\mathrm{s}(\varrho)/\ \|\boldsymbol{x}\| \leq \varrho)$, $c_k(s) \leq d_k(s)$ if $v_k < 0$ and $d_k(s) \leq c_k(s)$ if $l_k < 0$

$$s + v_k d_k(s) \leq 0 \quad (13)$$

For simplicity in the followings we assume: $d_k(s) = c_k(s) = s$ (s represents a generic independent scalar variable), then the state vector will be $\boldsymbol{x} = [x, y, z, v_x, v_y, v_z]^T$. If the state variables were all the same physical dimension, one could use the norm of the vector directly in the functional *V*, so one needs to introduce a suitable constant. A time constant T to multiply the velocity is used here:

$$V(t,x) = \frac{1}{2}(x^2 + y^2 + z^2 + T^2v_x^2 + T^2v_y^2 + T^2v_z^2) \quad (14)$$

In this way considering also the linearized dynamics

$$D^+V(t,\boldsymbol{x}) = xv_x + yv_y + zv_z + \beta_1T^2xv_x + \beta_2T^2yv_y + \beta_3T^2zv_z \leq \gamma\frac{1}{2}\big(x^2 + y^2 + z^2 + T^2v_x^2 + T^2v_y^2 + T^2v_z^2\big) \quad (15)$$

γ was introduced in place of $\gamma\frac{l_k}{\Delta t_k}$. Manipulating the inequalities, one obtains the equations of in the form of:

$$\boldsymbol{x^T A x} \geq \mathbf{0} \quad (16)$$

where $\boldsymbol{A}$ contains the coefficients of the associated polynomials. One needs to consider the coefficients of the matrix to find the solution of the problem. Considering only pairs (x-v_x), (y-v_y), (z-v_z) one obtains equations in the form:

$$\gamma x^2 - 2(1 + \beta_1T^2)xv_x + \gamma T^2v_x^2 \leq 0 \quad (17)$$

It follows that

$$\gamma \leq \max\left([(1 + \beta_1T^2), (1 + \beta_2T^2), (1 + \beta_2T^2)]\right) \quad (18)$$

At this stage, we introduce the controller, which can only modify the components of the velocity, and not all the components of the state variable, on the contrary of [RD 8].

The approach for this controller is based only on both position and velocity error $\boldsymbol{u}_k(\delta\mathbf{x}) = [0,0,0, -ax - av_x\ , -ay - bv_y\ , -az - bv_z\ ]^T$.

In this case the time constant is coincident with the time interval and it is user set. The value of l_k and γ is the same as before. The variation of the functional due to the manoeuvre is then:

$$\boldsymbol{V}(t_k^+, x + u_k) = \frac{1}{2}\big(x^2 + y^2 + z^2 + T^2(v_x + ax + bv_x)^2 + T^2\big(v_y + ay + bv_y\big)^2 + T^2(v_z + az + bv_z)^2\big) \leq \gamma\frac{1}{2}\gamma\frac{1}{2}(x^2 + y^2 + z^2 + T^2v_x^2 + T^2v_y^2 + T^2v_z^2) \quad (19)$$

Again considering state components pairs:

$$v_k^2 - v_k\ (a^2T^2 + b^2 - 2b) - a^2T\text{^}2 \leq 0 \quad (20)$$

Of which only the negative solution was retained. In this case the resolution was performed numerically minimizing the term $-(1 + v_k\ )$, subjected to the constraint $\gamma\Delta t_k + v_k\ \leq 0$. Analysing the discrete LQR we noted the fact that

the proportional coefficient was always circa 1, so we imposed *b* to be equal to 1. This value is sensible, given that in the case of zero position error, the condition which assures a zero velocity error is to impose a delta-v correction of the same magnitude but in the opposite direction. We then add the integrative term shown for the discrete LQR.

4. NAVIGATION MODELS

The navigation capabilities of HADES are based on two trajectory estimation routines

1. A performance model based on typical knowledge of the spacecraft trajectory.
2. A real-time on board filter based on the Unscented H-infinity Filter (UHF) which uses LIDAR and camera measurements.

The H_∞ filter was selected because it does not require prior assumptions on the nature of the noise, and minimizes the worst-case estimation error. The choice of the H_∞ filter is preferable when the Gaussian hypothesis cannot be fully guaranteed, for example when biases in the instruments are not detected [16]. In our case, besides biases affecting all the instruments, the LIDAR measurements are affected by the camera process and errors. Therefore, the noise introduced by the LIDAR cannot be modelled as an uncorrelated white noise.

In order to deal with nonlinearities, one can use an extension to the H_∞ filter, the Extended H_∞ Filter (EHF), analogous to the extended Kalman filter. In this case, however, some hypotheses need to be introduced on the smoothness and regularity of the process and measurements. An alternative is to introduce the unscented transformation in the H_∞ filter to avoid the approximation of the Jacobian matrices [17] and build an Unscented H_∞ Filter.

4.1. Instruments model

We considered a camera and a LIDAR as on-board instruments. In particular, for the camera we used the pinhole model of [18] to identify the centre of brightness $[x_c^c, y_c^c] = [u_c^c, v_c^c]p_{width}$ converted into azimuth and elevation angles:

$$\begin{aligned} \phi &= \tan^{-1}\frac{x_c^2}{f} \\ \psi &= \tan^{-1}\frac{y_c^2}{\sqrt{(x_c^c)^2+f^2}} \end{aligned} \tag{21}$$

where *f* is the focal length of the camera.

In general, the LIDAR provides range from the spacecraft to a point on the surface of the target object and works at a range from 50 m to 50 km. It is assumed that the LIDAR illuminates the point on the surface that corresponds to the centroid derived from the elaboration of the images acquired by the camera ([19]). This distance is simply given by:

$$l = \left\| \delta \boldsymbol{r}_{SC} - \boldsymbol{x}_{surface}^c \right\| \tag{22}$$

where $\boldsymbol{x}_{surface}^c$ is the position of a point on the asteroid's surface along the centroid direction.

The actual illumination and visibility condition are considered such that the image on the screen of the camera will be as shown in an example of Figure 3 (1), where the centre of brightness along with the centroid and the barycentre has been represented. Figure 3 (2) shows the footprint of the LIDAR on the surface as taken around the centre of brightness of the previous example

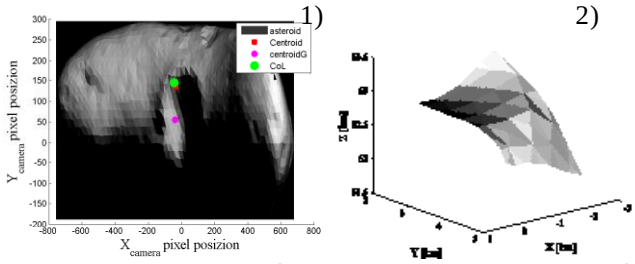

Figure 3. Example of image as seen on the screen of the camera and footprint of the LIDAR.

5. DEFLECTION MODELS

This section describes the deflection techniques and long period propagation features which are used by HADES.

5.1. Laser ablation

The laser-matter interaction model aims at computing the momentum imparted to the asteroid as a function of its physical and dynamical properties as well as the key parameters of the laser system, namely the output power and the focusing capabilities. The calculation of the thrust generated was taken from [20], where a complex 3D model employing time variable. Namely, the figure of merit is given by the momentum coupling coefficient, representing the amount of thrust one gets per optical watt of power invested in the process:

$$C_m(t) = \frac{T}{P} = \frac{p_e + \rho_e v_e^2}{\Phi} = \frac{(\gamma+1)p_e}{\Phi} \tag{23}$$

where the pressure p_e and velocity v_e in the gas on the edge of the Knudsen layer (between the liquid and gas phase) the effective pressure and the flux Φ:

An example of momentum coupling computed by the model for an S-type asteroid is represented in Figure 4 as a function of the laser system parameters and assuming a local surface speed of 10 cm/s.

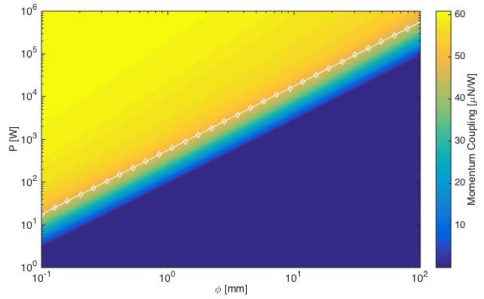

Figure 4. Momentum coupling as a function of the focusing and optical power (credits [19]).

5.1.1. Pointing strategies

If one neglects the possibility to control the asteroid rotation, different pointing strategies could be used. Two alternative strategies were explored:

1. the laser is pointed such that the resulting thrust will be as much as possible aligned with the desired deflective action (for example along the orbit tangent which maximizes the overall displacement).

$$\max_{\mathbf{s}} cos(\widehat{\mathbf{n}(\mathbf{s}), \mathbf{n}_{\text{desired}}}) \quad (24)$$

   where $\mathbf{n}$ is the local normal – which gives the direction of the resulting thrust – and $\mathbf{n}_{\text{desired}}$ is the desired normal. An example of this process can be seen in Figure 5 (1) where the laser is placed along the y-axis.
2. the laser is pointed in a fixed direction towards the asteroid. The intersection point is identified as the barycentre of the triangle of the asteroid mesh closest to spacecraft position vector $\mathbf{r}_{SC}$. In practice:

$$\max_{\mathbf{s}} cos(\widehat{\mathbf{s}, \mathbf{r}_{SC}}) \quad (25)$$

   An example of the implemented procedure is shown in Figure 5 (2), where the red areas represent the closest points to the laser beam (the laser is placed along y-axis).

5.2. Ion beam shepherd

The ion beam shepherd method is based on the use of low thrust engines directed against the asteroid. At the same time a second thruster pushes the spacecraft in the opposite direction, thus maintaining the spacecraft position. The flow of exhausted ions exerts a small pressure on the surface, which in turns produces a force on the asteroid.

The model of IBS used in this preliminary development considers simplified assumptions on the expansion of the ion flow outside of the thruster exit plane where the exit velocity is much greater than the radial velocities and the ion sound speed.

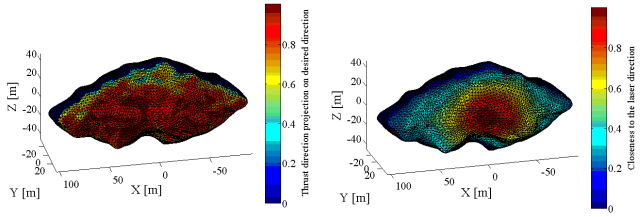

Figure 5. Laser control 1) surface points producing an effective thrust directed in the desired one, 2) points closer to the laser beam direction. Note that the two colour-bars refer to different concept.

The assumption of the model is that the ion beam profile starts out and remains a Gaussian profile. The behaviour can be described as in [21], in terms of thruster characteristics of thrust T, specific impulse I_{sp}, ion beam temperature T_e and propellant atomic mass M_a.

The force acting of the surface of the asteroid can be calculated as the discrete sum of forces produced by the ion dynamic pressure on each visible element of the mesh at the location (r,z) of normal $\mathbf{v}$:

$$\mathbf{F}_{\text{IBS}} = \sum 0.5\,\rho(r,z)v^2(r,z)dS(r,z)\mathbf{v} \quad (26)$$

An example of force distribution is shown in Figure 6, where the thruster is placed at 200 m from the asteroid and pointed towards it along the y-axis.

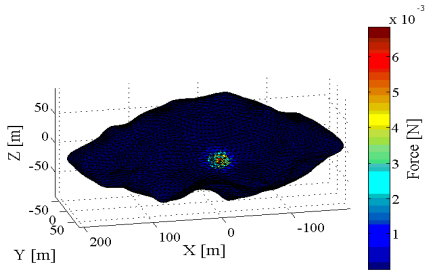

Figure 6. IBS force distribution on the asteroid surface.

5.3. Gravity tractor

Conceptually the gravity tractor is the simplest deflection method. The resulting thrust is simply exerted by the gravity acceleration multiplied by the spacecraft mass M_{SC}:

$$\mathbf{F}_{\text{GT}} = M_{SC}\frac{\mu_a}{r^3}\mathbf{r} \quad (27)$$

where the resulting force is directed along the asteroid spacecraft direction. Note that in an ideal inertial hovering

configuration a couple of thrusters needs to be off-pointed from the asteroid such that the flow will not impinge on the asteroid. In this way the total magnitude of the thrust will be:

$$\mathbf{T}_{\mathrm{tot}} = \frac{\mathrm{F_{GT}}}{\sin(\tan^{-1}\frac{\mathrm{R_{max}}}{\mathrm{r_{SC}}}+\frac{1}{2}\varphi_{\mathrm{cone}})} \qquad (28)$$

where $\tan^{-1}\frac{\mathrm{R_{max}}}{\mathrm{r_{SC}}}$ represents the half field of view occupied by the asteroid and φ_{cone} is the expansion cone of the thrusters. In this way given the power available for deflection, one can calculate the total thrust and the mass of the spacecraft.

5.4. Long period propagation

While the target delta-velocity is independent of the direction of thrust, the effect on the displacement from its nominal position at a given point along the orbit (called check-point in the following) depends on the direction of the thrust.

Let a, e, i, Ω, ω_a and M_a be respectively semi-major axis, eccentricity, inclination, right ascension of the ascending node, argument of the pericentre and mean anomaly of the nominal orbit of the asteroid. The effect of the deflection is calculated at predefined check-points. Let t_{check} be the instant of time corresponding to a generic check point.

If θ_{check} is the true anomaly of the asteroid, and $\theta^*_{check} = \theta_{check} + \omega_a$ the corresponding argument of latitude, one can write the variation of the position of the asteroid after deviation, with respect to its unperturbed position, by using the proximal motion equations as in [22] and [23]:

$$\delta\boldsymbol{r}_a(t_{check}) = \boldsymbol{A}_{check}\delta\boldsymbol{\alpha}(t_{check}) \qquad (29)$$

where $\delta\boldsymbol{r}_a = [\delta x_{\mathrm{h}-a}, \delta y_{\mathrm{h}-a}, \delta z_{\mathrm{h}-a}]$ with $\delta x_{\mathrm{h}-a}$, $\delta y_{\mathrm{h}-a}$ and $\delta z_{\mathrm{h}-a}$ the displacements in the radial, transversal and out of-plane directions in the Hill's reference frame centred at the unperturbed position of the asteroid at the check point (see [23]). $\delta\boldsymbol{\alpha}(t_{check}) = [\delta a, \delta e, \delta i, \delta\Omega, \delta\omega_a, \delta M_a]$ is the variation of the orbital parameters at the check-point and the matrix $\boldsymbol{A}_{check}$ transforms the variation of the orbital parameters in trajectory displacements. In this way one can compute the effect of the deflection action at the check-point $t_{check} = t_e$.

In order to perform fast simulations we used averaged quantities within Eq. (29) exploiting the fact that on several rotations the mean direction and the fraction of useful thrust as well as the imparted angular velocity variation will depend on the shape of the asteroid, angular velocity and relative position of the deflection system.

6. EXAMPLES

6.1. Asteroid Didymos

For the sake of brevity, we will just show some results applied to the body fixed and inertial hovering cases in the Hill's frame, given that the pure inertial one differs only slightly with respect to the Hill's case.

In the following, the analysed methods are tested. Besides the calculation of mere control figures as the navigation budget, the comparison is based also on the capability to control the spacecraft with a limited number of actuations. The asteroid selected was the main body of the binary asteroid Didymos, whose Keplerian elements in the Sun ecliptic frame are [24]:

$$[a\ e\ i\ \omega\ \Omega] = [1.644364375\mathrm{AU}, 0.383635, 3.4078\ \mathrm{deg}, 73.2396\ \mathrm{deg}, 319.2468\ \mathrm{deg}]$$

The motion of the asteroid around the Sun is purely Keplerian without any perturbation and simulations start from perigee. The asteroid was assumed to be shaped as a tri-axial ellipsoid of semi-axes:

$$[\mathrm{c_1}\ \mathrm{c_2}\ \mathrm{c_3}] = [1.05\ 0.65\ 0.45]\mathrm{km}$$

These figures have been drawn from the available estimate of the mean radius, i.e. 0.75 ± 0.1 km (1σ). The gravity constant from the asteroid is $3.516{\cdot}10^{-8}$ km/s^3 [24]. The asteroid rotates at the speed of 2.259 *rph* around $\mathrm{c_3}$ axis, with the equatorial plane coincident with the asteroid orbital plane. Assuming such a shape allows calculating the C_{20}, C_{22}, C_{40}, C_{42}, C_{44} gravitational harmonics analytically.
The spacecraft is assumed to have a ballistic coefficient of 0.0393 m^2/kg and an equivalent reflectivity coefficient (given by reflection and diffusion) of 1.3.

For what concerns the analysis for body fixed and inertial hovering of following Sections 6.1.1 to 6.1.3., we considered the following actuation errors – 5% error (3σ) on magnitude and 2 degrees on angles (3σ). For the navigation we used the performance model where the pseudo state vector was known with 20 m along track, 10 m cross track in position and 2 mm/s along track and 1 mm/s cross track in velocity (all the quantities are 3σ).

6.1.1. Body fixed hovering

For this asteroid the spacecraft cannot fly on a synchronous orbit because this falls well below the asteroid's surface. Given the weak gravity field of the asteroid, its orbit radius would be in fact roughly 300 m.

So we considered three initial nominal conditions of the spacecraft. For conciseness we report just an example where

the nominal spacecraft position is at 200 m above the surface along c_1 direction with null relative velocity

$$[x \quad y \quad z \quad v_x \quad v_y \quad v_z] =$$
$$[1.25\text{km} \ 0.00\text{km} \ 0.00\text{km} \ 0\text{km/s} \ 0\text{km/s} \ 0\text{km/s}]$$

Results are reported for one day of operations at the asteroid. An initial random error in the range of 100 m in position and 1 cm/s in velocity per components was used. We show the results in terms of position error, excluding reflection methods which are highly inaccurate to pursue a body fixed mission at low altitude.

Figure 7 shows the trend of the error in the controlled position. For the discrete controllers, the error is shown for maximum interval of time where the control is able to maintain the spacecraft above the surface. For the control box and dead band controller half side of the box was set to 100 m. It is clear that these two methods result to be less accurate because of linearization assumption which cannot include the Coriolis effects properly. In fact at the assumed angular velocity the contribution of the gravity force becomes less noticeable with respect to the Coriolis acceleration which varies considerably within 200 m. On the contrary the discrete LQR is quite accurate for 1200 s control time, although an initial overshooting due to high initial errors. The better accuracy is due to the fact that gains are calculated considering how the variation of velocity affects the other components.

Table 1 shows a synthetic comparison for the control budget in this configuration. It is apparent that the discrete LQR is the best choice both in terms of accuracy and Δv budget within the discrete controllers.

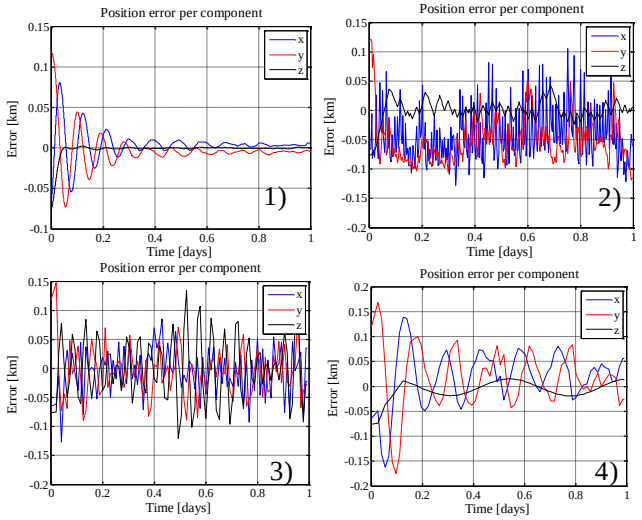

Figure 7. Control error for 1) continuous thrust 2) control box with 300 s sampling time 3) dead-band with 900 s sampling time and 4) 1200 s discrete LQR.

For this reason we focus now on the discrete LQR. Figure 8 shows an example of Δv budget for different body fixed hovering conditions and different actuation intervals. Three cases were considered:

1. Case 1 corresponds to the hovering condition along c_1 of previous analyses.
2. Case 2 sees the spacecraft at 200 m above the surface along c_2 direction with null relative velocity
   $[x \quad y \quad z \quad v_x \quad v_y \quad v_z] =$
   $[0.\text{km} \ 0.85\text{km} \ 0.00\text{km} \ 0\text{km/s} \ 0\text{km/s} \ 0\text{km/s}]$
3. Case 3 maintains the spacecraft in a particular position with null relative velocity
   $$[x \quad y \quad z \quad v_x \quad v_y \quad v_z] =$$
   $$[0.75\text{m} \ 0.75\text{km} \ 0.75\text{km} \ 0\text{km/s} \ 0\text{km/s} \ 0\text{km/s}]$$

Table 1. Body fixed hovering for spacecraft placed along c_1 axis: synthetic comparison

Method	Actuation interval	Δv [m/s]
Continuous thrust	5	56.2
Control box	300	62.5
Dead-band control	300	64.3
	600	61.7
	900	54.4
Discrete LQR	300	55.8
	600	54.9
	900	53.4
	1200	51.2

As one can see the control Δv decreases as the actuation time intervals increase. Care needs to be placed, since the 1200 s is the limit which guarantees no crash conditions for Case 1.

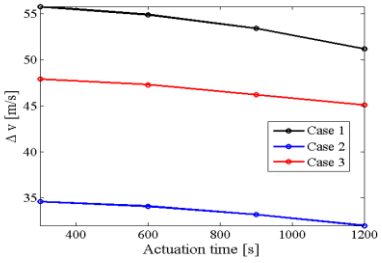

Figure 8. Example of Δv budget for three different body-fixed hovering conditions using discrete LQR.

6.1.2. Inertial hovering

The initial nominal condition of the spacecraft was randomly generated around the nominal operational trajectory in the local Hill's frame (radial, tangential and out of plane components) and then converted to asteroid inertial frame:

$$[x \quad y \quad z \quad v_x \quad v_y \quad v_z\ ] = [-3.423km\ 0.05km\ 0.05km\ 0.000031km/s - 0.000051km/s \quad 0.000020km/s\ ]$$

Besides the calculation of mere control figures as the navigation Δv budget, the comparison is also based on the capability to maintain the illumination angle (given by Sun-asteroid-SC angle) below 5 degrees. For simplicity in Figure 9 we report the trend for the illumination angle for all the analysed cases. Besides the initial transient, some methods results more effective in maintaining the spacecraft within the 5 degrees boundaries. In particular the continuous one is the most precise, while the 6 hrs LQR is the most precise among the discrete controllers.

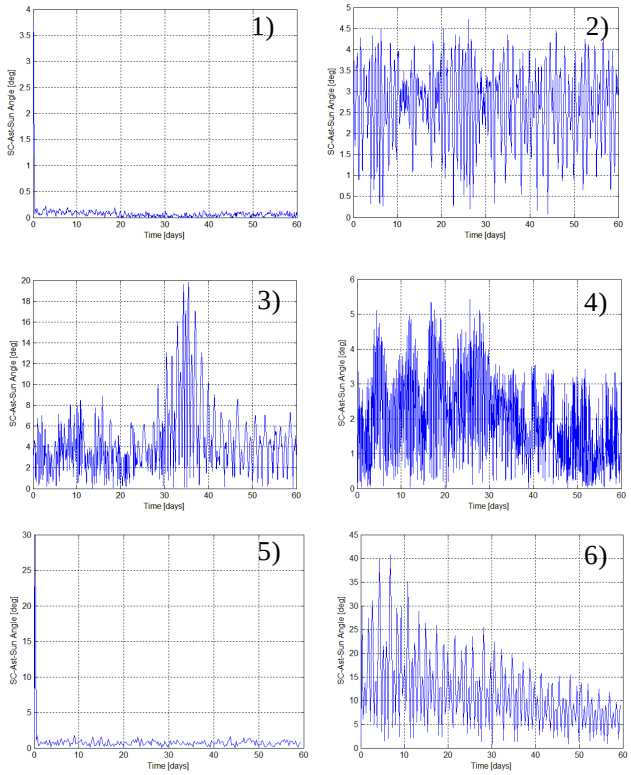

Figure 9. Illumination angle for 1) continuous thrust, 2) control box, 3) reflection method, 4) dead-band control, 5) 6 hours discrete LQR and 6) 6 hours stable PD.

Table 2 reports the navigation Δv budget for the different controllers. Considering the above results, one may always refer to the compliance to the control requirements to select the correct controller. In particular the reflection method fails to respect the requirements, but in pre-orbit acquisition phases this method can be used because it does not require very precise navigation system [9].

One can see that the minimum actuation time is the lowest for the dead-band method. This is essentially due to the fact that the control along it is performed only when required on per component basis. This means that control firings could be necessary along one direction at a certain instant *k* but it might be required to fire again along another direction at the subsequent *k+1* instant. .

Table 2. Inertial hovering control methods: synthetic comparison

Method	Actuation interval (min-max-mean) [min]	Δv [m/s]
Continuous thrust	8	16.9
Control box	421/533/485	24.2
Reflection method	325/1792/890	11.2
Dead-band control	8/440/140	25.9
Discrete LQR	360 (fixed)	24.1
Discrete LQR	240 (fixed)	24.0
Discrete LQR	180 (fixed)	23.1
Stable PD	360 (fixed)	18.2
Stable PD	240 (fixed)	18.2
Stable PD	180 (fixed)	18.2

This is an undesired effect, which is advisable to avoid, at the cost of higher propellant consumption. The reflection method presents the highest maximum actuation interval. This comes from the fact that the spacecraft is inserted into high eccentricity orbit because of the accumulation of actuation and orbit determination errors.

The stable PD with 1-2-3 hours control interval does not present similar drawbacks. Moreover the overall consumption is also comparable to the fixed and variable magnitude controllers, which keep the spacecraft within 5 deg illumination angle.

The discrete LQR and stable PD with the integrative contribution show very good performances, and both are able to maintain the spacecraft with one actuation every 6 hours. Although one cannot achieve good results in terms of illumination angle, the spacecraft does not leave the proximity or impact on the asteroid. Anyway LQR shows better convergence properties but at higher propellant consumption.

6.1.3. MC example

For simplicity we considered a case analysed during a study carried out for ESA's AIM mission, where the spacecraft was placed in a fixed hovering configuration:

$$x_0 = 5 \cdot [-1km, 1km, \sqrt{2}km, 0km/s, 0km/s, 0km/s]$$

It was needed to maintain it within a 1.5 km side control box for 60 days.

For this purposes the selected controller was based on the discrete control box method. Figure 10 shows an example for the station keeping of the AIM.

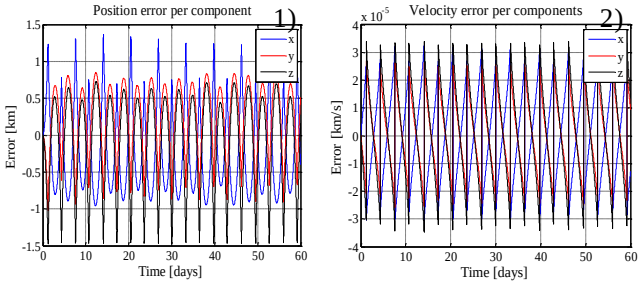

Figure 10. Control box: 1) position and 2) velocity errors for AIM during 60 days period.

One can appreciate how manoeuvres on three directions are performed at the same time in order to reduce the number of actuations (see Figure 1111).

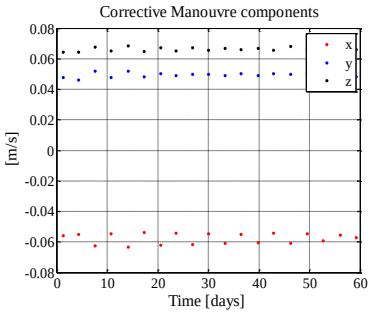

Figure 11. Control manoeuvres per components.

For the MC simulations we considered 100 samples propagated for 30 days. The initial conditions were affected by an initial dispersion in position of 50 m per component, and in velocity of 1 cm/s (1σ). The manoeuvres were affected by a 2% (3σ) error in magnitude and 1.5 deg (3σ) error in direction.

The results of the simulation as displayed by HADES are reported in Figure 12 together with main statistical parameters. One can see that the minimum actuation time will be about 2.7 days, which can help identifying the time interval between ground operations to comply with the control requirements. This mere figure could not be drawn from a single simulation perturbed simulation. Also the worst case Δv budget will be in the range of 2 m/s. For convenience in Figure 13 we report the distribution of experiments, where it is possible to see also the minimum correction manoeuvre magnitude as a function of minimum actuation time. This can be also used to identify possible requirements of the control thrusters.

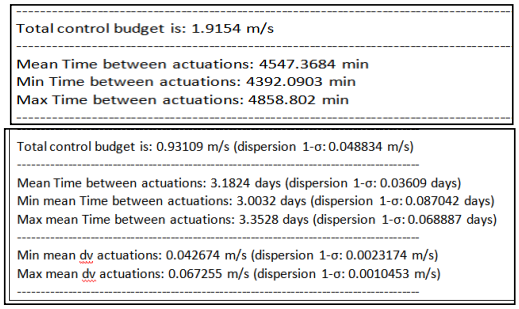

Figure 12. MC analysis: synthetic results displayed.

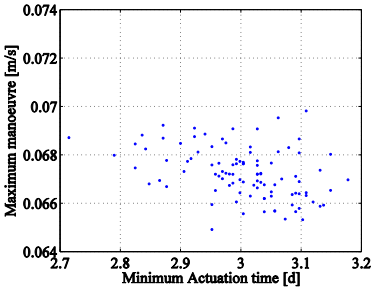

Figure 13. MC analysis: maximum manoeuvre magnitude vs. minimum actuation time.

6.1.4. Inertial hovering navigation performance

In this section, we want to show how different dynamic and measurement models affect the performance of the state estimate along with the navigation Δv budget. We selected again asteroid Didymos, without considering the effects from its moon. Note that lacking of actual shape data, we used different mesh maps from asteroid (433) Eros.

Table 3 reports the characteristics of the sensors assembly:

Table 3. Measurements assembly characteristics

Lidar mounting error (1σ)	0.001 deg
Lidar range error (1σ)	10 m
Lidar range bias (1σ)	1 m
Number of pixels per side	2048
Camera FoV	20 deg
Camera side	10 cm
Attitude error (1σ)	0.0057 deg
Attitude bias (1σ)	0.0006 deg

The simulation was carried out for 3 days. The initial estimation error was 100 m and 1 cm/s for each position and velocity components, respectively.

We start with an ellipsoidal shape case where the gravity field for the real world is generated through the shape model, while the gravity field is truncated to the 4th order in

the filter. We used the simple measurements model of Section 4. Figure 14 shows that the measurements tends to be biased on 3-axis for the position estimate.

The second case differs from the first one in that we used the detailed measurements model. Figure 15 shows that the error per component is accentuated with respect to the ones in Figure 14.

In the third case we considered the same shape model for both the real world and the filter, with the detailed measurements model. We used 1708 facets mesh from the asteroid (433) Eros. As one can reasonably expect, from Figure 16 the convergence towards zero region error is quite smooth, because of the full knowledge of the environment.

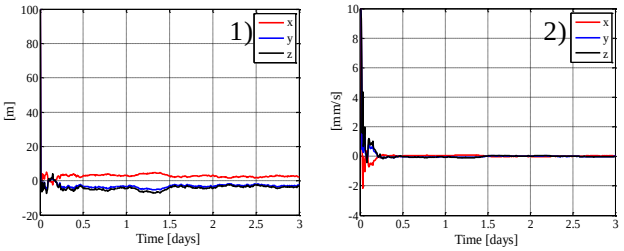

Figure 14. Ellipsoid shape, 4th order filter gravity field and simple measurements model: estimation error.

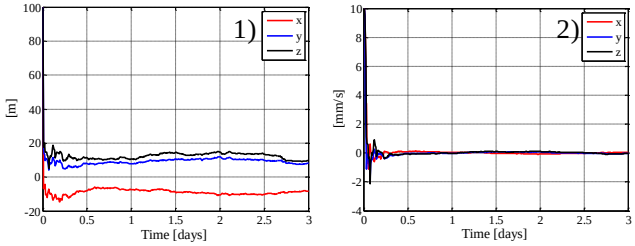

Figure 15. Ellipsoid shape, 4th order filter gravity field and detailed measurements model: estimation error.

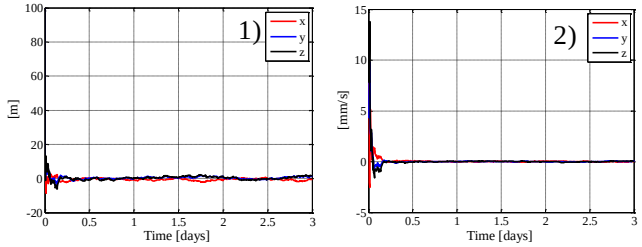

Figure 16. 1708 facets for real world and filter, and detailed measurements model: estimation error.

An additional case was executed where we used different shape models in the real world and in the estimated world. In the filter we used 1708 facets mesh while the actual dynamics was based on 7790 facets. Moreover the actual mean radius was decreased by about 1% that is about 6 m. This affected both the dynamics and measurement model. In fact from Figure 17, we can see that the error converges to a region where a clear asymptotic behaviour cannot be spotted, except for the velocity error.

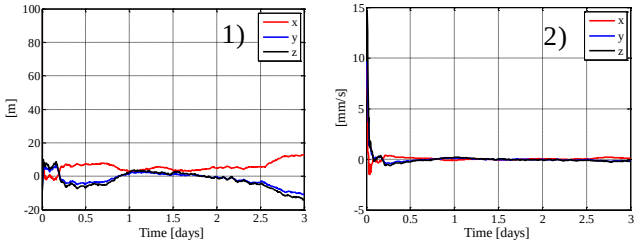

Figure 17. 7790 facets for dynamics and 1708 facets for filter, and detailed measurements model: estimation error.

The effect on the Δv budget for the different cases is reported in Table 4. Note that in 3 days only one manoeuvre has been performed.

Table 4. Measurements assembly characteristics

	Δv [cm/s]
Case 1	9.18
Case 2	9.14
Case 3	9.25
Case 4	9.18

In general the difference is about 10% but Case 3 represents the actual need for the control, being the estimation more accurate.

6.2. Deflecting a 100 asteroid

For this exercise, we considered the shape of asteroid (433) Eros scaled down to 100 m mean diameter. In this way the total asteroid mass was $9.263 \cdot 10^8$ kg. We considered deflection operation lasting 20 years with a maximum power only for deflection (laser system or thrusters) limited to 20 kW. We considered around 60% efficiency for the thrusters. Note that given the lack of a mass model, the laser ablation and IBS cases do not consider the possible reduction in thrust due to the attractive force given by the spacecraft mass itself. For this comparison we neglected the contamination model, which has not been included in the case of the IBS.

Figure 18 shows the total deflection achieved using the different pointing strategies with the laser ablation. With respect to operation lasting 20 years, the fixed pointing is 20% less efficient than the variable thrust one. However, the former is conceptually simpler than the latter, not requiring to adjust the attitude or a mechanism at the laser.

Similar results in terms of shape are achieved using the IBS, as shown in Figure 19 (1). We see that the achieved deflection is about 50% less efficient than the one in the variable laser pointing and 40% with respect to the fixed pointing. However, this analysis does not take into account several factors such that the actual efficiency of the LA system, the mass of the system and other power units which favours the IBS over the LA system. Moreover the LA is considerably strongly affected by the contamination due to the ejecta plume which will strongly reduce the power available during several years of operations (see [25] for details).

Finally Figure 19(2) reports the same analysis for the gravity tractor. We placed the spacecraft at 200 m and considered a 12 degrees divergence angle for the thrusters.

Apparently the gravity tractor is the one permitting to achieve the highest deflection (more than 80 Earth radii) but if one calculates the required mass it results that a 16500 kg spacecraft placed at 200 m would be required. This is of course beyond current technological launch limits.

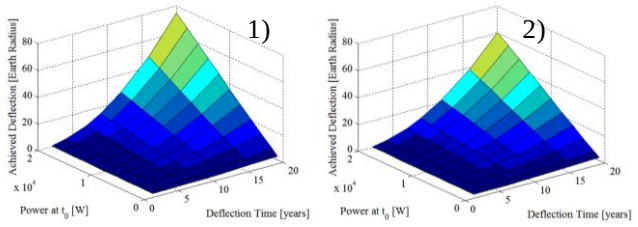

Figure 18. LA deflection: 1) controlling laser pointing, 2) maintaining laser pointing fixed.

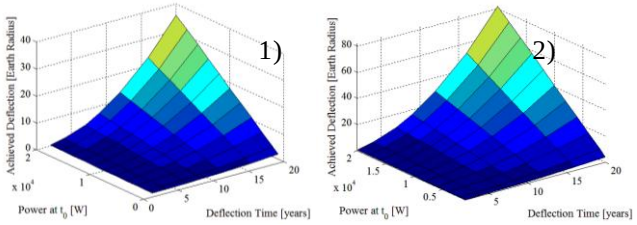

Figure 19. 1) IBS deflection and 2) GT deflection.

6.3. Debris analysis

Although primary goals of HADES are set to analyse GNC operations and asteroid deflections, it can be also used to assess the stability of the orbits close to the irregular bodies. In particular, we used it to assess when the area near the small 100 m asteroid of the previous section can be considered clear by any debris after a hypothetical precursor impacting mission. We did not model the impact itself but we assumed that all the particles with energy above the escape one would soon leave the asteroid proximity.

We generated about 30,000 uniformly distributed particles on the surface of the asteroid with $E \leq 0$ in all direction for different area to mass ratios. Figure 20 reports the trend for two different values of area to mass ratios (A2M), and fractions of the asteroid's nominal angular velocity (where the parameter k_ω is the factor dividing the angular velocity).

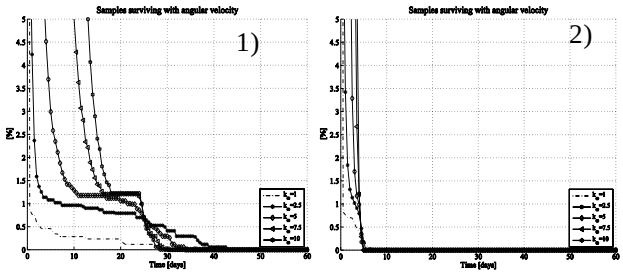

Figure 20. Debris analysis for 1) A2M = 0.001 kg/m^2 and (2) A2M = 0.01 kg/m^2

The criteria used to count the surviving samples were set as the samples neither impacting nor leaving the asteroid proximity. The leaving condition coincides with the particle moving outside the Hill's radius that for the considered asteroid was circa 15 km. The initial conditions play an important role in the number of surviving particles; if the A2M is the same, particles with lower initial tangential velocity will have more probability to survive for longer periods (also truth that we used 2-body U, instead of the actual energy of single point).

The SRP will affect the survivability - in fact A2M = 0.001 kg/m^2 produces more surviving samples because particles are more affected by the asteroid's gravity and less by the SRP.

7. CONCLUSIONS

This paper presented the main features of the High-fidelity Asteroid Deflection Evaluation Software developed at Deimos Space S.L.U. for close proximity operations and deflection purposes.

The software can deal with inertial and body fixed hovering configurations, considering different control strategies. Navigation capabilities are also integrated in terms of a performance model or in terms of a filtering capability. It is possible to perform the analyses using different models for the actual dynamics (real world) and one for the estimated world. In this way one can assess how the knowledge of the environment affects the navigation and the control budget. We showed and compared several examples of body-fixed hovering and we focused on the navigation performance for different levels of environment

knowledge, assuming shape and harmonics models for the gravity field.

A Monte Carlo module permitted us to calculate relevant statistics for an inertial hovering at Didymos. Note that in future updates we are planning to consider also the gravitational perturbation from a possible moon around the asteroid.

We also demonstrated that HADES can be used to perform debris analysis, assessing when close proximity operations can start in case of some impacting mission hitting the surface of a 100 m asteroid.

We showed that HADES can perform preliminary deflection analyses for LA, IBS and GT, under simplified analysis. In fact we compared the different methods without considering the actual mass of the LA and IBS system. In particular we did not consider the power loss for the laser system, but only the output optical power.

In order to have a correct picture of the deflection action, there are already a number of features under development, which are basically the integration of the deflection techniques into the GNC modules. In this way a detailed model of the different techniques will allow identifying preliminary navigation requirements and allow fully simulating the deflection operations. It will be necessary to integrate the deflective acceleration acting on the asteroid, and possibly integrate an onboard estimation for it.

It is also planned to integrate a contamination module due to the ejecta plume for the laser and the back-sputtering for the IBS. The contamination affects the power available during the lifetime. As an example, Figure 21 reports the achieved deflection for the laser variable pointing case. The contamination due to the plume can produce a reduction of 60% with respect to the ideal case.

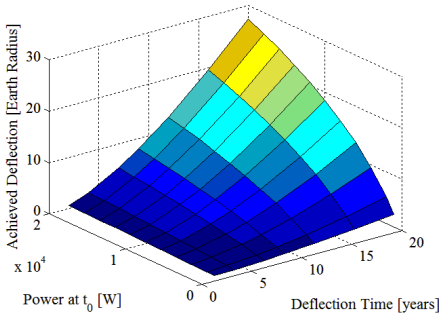

Figure 21. Laser ablation deflection controlling laser pointing with contamination due to the plume of ejecta.

9. ACKNOLEGEMENTS

The present tool has been developed within the European Commission's Framework Programme 7 funded Stardust project, through the Stardust Marie Curie Initial Training Network, FP7-PEOPLE-2012-ITN, Grant Agreement 317185.

10. REFERENCES

[1] T. Morley, F. Budnik, "*Rosetta Navigation for the fly-by of the asteroid 2867 Steins*", Proceedings of the 21st International Symposium on Space Flight Dynamics. Toulouse, France, 2009.

[2] D.J. Scheeres, R. Gaskell, S. Abe, O. Barnouin-Jha, T. Hashimoto, J. Kawaguchi, T. Kubota, J. Saito, M. Yoshikawa, N. Hirata, T. Mukaik, M. Ishiguro, T. Kominato, K. Shirakawa and M. Uo, "*The Actual Dynamical Environment About Itokawa*", AIAA/AAS Astrodynamics Specialist Conference and Exhibit, Keystone, Colorado, 21 - 24 August 2006.

[3] D.J. Scheeres, S. Broschart, S.J. Ostro and L.A. Benner, "*The Dynamical Environment About Asteroid 25143 Itokawa: Target of the Hayabusa Mission*", AIAA/AAS Astrodynamics Specialist Conference and Exhibit. Providence, Rhode Island 16 - 19 August 2004.

[4] T. Kubota, T. Hashimotoa, S. Sawai, J. Kawaguchib, K. Ninomiyaa, M. Uoc, K. Babac, "*An autonomous navigation and guidance system for MUSES-C asteroid landing*", Acta Astronautica 52 (2003) 125 – 131.

[5] S. Li, P. Cui and H. Cui, "*Autonomous navigation and guidance for landing on asteroids*", Aerospace science and technology, 10(3): 239-247, 2006

[6] H.J. Melosh, I.V. Nemchinov and Y.I. Zetzer, "*Non-nuclear strategies for deflecting comets and asteroids*", In: Gehrels, T. (Ed.), Hazard due to comets and asteroids. University of Arizona Press, pp. 1111–1132, 1994.

[7] C. Colombo, J.P. Sanchez Cuartielles, M. Vasile et al, "*A comparative assessment of different deviation strategies for dangerous NEO*", International Astronautical Congress. Valencia, Spain, October, 2006.

[8] A. Galvez et al, "Asteroid Impact Mission (AIM) & Deflection Assessment: An Opportunity to Understand Impact Dynamics and Modelling", European Planetary Science Congress 2012, in Madrid, Spain,23-28 September, 2012.

[9] Scheeres, D. J., *Orbital Motion in Strongly perturbed Environments. Applications to Asteroid, Comet and*

Planetary Orbiters. 1st edition, Springer-Praxis books in astronautical engineering. 2011

[10] Montenbruck, O. and Gill, E., *Satellite Orbits: Models, Methods and Applications*, Springer-Verlag, Heidelberg, 2005.

[11] T. Winkler, B. Kaplinger and B. Wie, "*Optical Navigation and Fuel-Efficient Orbit Control around an Irregular-Shaped Asteroid*", AIAA Guidance, Navigation, and Control (GNC) Conference, Boston, USA, 08/2013.

[12] W. Boyce, "*Comment on a formula for the gravitational harmonic coefficients of a triaxial ellipsoid*", Celestial Mechanics and Dynamical Astronomy, , Volume 67, Issue 2, pp 107-110, February 1997

[13] M. Vasile and C.A. Maddock. "*Design of a Formation of Solar Pumped Lasers for Asteroid Deflection*", Advances in Space Research, 2012, 50(7): 891-905, 2012

[14] S. B. Broshart and D. J. Scheeres. "*Boundness of Spacecraft Hovering under Dead-Band Control in Time-Invariant systems*", Journal of Guidance, Control and Dynamics Vol. 30, March-April 2007.

[15] Y. Liu et al., 2003. "*Stability Analysis of Impulsive control systems*", Mathematical and Computational Modelling 37 (2003) 1357-1370), 2003.

[16] Simons, D., *Optimal state estimation, Kalman, and Non-linear Approaches*, Published by John Wiley & Sons, Inc., Hoboken, New Jersey, 2006.

[17] W. Li, and Y. Jia, "*H-infinity filtering for a class of nonlinear discrete-time systems based on unscented transform*", Signal Processing 90(2010)3301–3307, 2010.

[18] S.M Oh and E.N. Johnson, "*Relative Motion Estimation for Vision-based Formation Flight using Unscented Kalman Filter*", AIAA Guidance, Navigation and Control Conference and Exhibit, Hilton Head, South Carolina, 2007.

[19] K. Dionne, "*Improving Autonomous Optical Navigation for Small Body Exploration Using Range Measurements*", AIAA 2009-6106. AIAA Guidance, Navigation, and Control Conference, 10 - 13 August 2009, Chicago, Illinois.

[20] N. Thiry and M. Vasile, "*Deflection of uncooperative targets using laser ablation*", in SPIE Optical Engineering + Applications. International Society for Optics and Photonics, 2015.

[21] Goebel D. M. and Katz Ira. *Fundamentals of Electric Propulsion: Ion and Hall Thrusters*, JPL SPACE SCIENCE AND TECHNOLOGY SERIES. Chapter 1 and 8., March 2008.

[22] M. Vasile and C. Colombo, "*Optimal impact strategies for asteroid deflection*", Journal of Guidance, Control and Dynamics, vol. 32, no. 4, pp. 858–872, 2008.

[23] C. Colombo, M. Vasile and G. Radice, "*Semi-Analytical Solution for the Optimal Low-Thrust Deflection of Near-Earth Objects*", Journal of Guidance Control and Dynamics 32(32):796-809, May 2009.

[24] http://ssd.jpl.nasa.gov/sbdb.cgi?sstr=65803+Didymos

[25] M. Vetrisano et al, "*Asteroid's Orbit and Rotational Control Using Laser Ablation: Towards High Fidelity Modelling of a deflection Mission*", in 25th International Symposium on Space Flight Dynamics, Munich, Germany, October 19-23, 2015.